

1

2       **Transport Above the Asian Summer Monsoon Anticyclone**

3               **inferred from Aura MLS Tracers**

4

5

6

7               Mijeong Park<sup>1</sup>, William J. Randel<sup>1</sup>, Andrew Gettelman<sup>1</sup>,

8               Steven T. Massie<sup>1</sup> and Jonathan H. Jiang<sup>2</sup>

9

10              <sup>1</sup>National Center for Atmospheric Research

11                              Boulder, Colorado

12              <sup>2</sup>Jet Propulsion Laboratory, California Institute of Technology

13                              Pasadena, California

14

15

16

17

18                              Revised April 2007

19

20

21

22

## Abstract

Tracer variability above the Asian summer monsoon anticyclone is investigated using Aura Microwave Limb Sounder (MLS) measurements of carbon monoxide, ozone, water vapor and temperature during Northern Hemisphere summer (June to August) of 2005. Observations show persistent maxima in carbon monoxide and minima in ozone within the anticyclone in the upper troposphere - lower stratosphere (UTLS) throughout summer, and variations in these tracers are closely related to the intensity of underlying deep convection. Temperatures in the UTLS are also closely coupled to deep convection (cold anomalies are linked with enhanced convection), and the three-dimensional temperature patterns are consistent with a dynamical response to near-equatorial convection. Upper tropospheric water vapor in the monsoon region is strongly coherent with deep convection, both spatially and temporally. However, at the altitude of the tropopause, maximum water vapor is centered within the anticyclone, distant from the deepest convection, and is also less temporally correlated with convective intensity. Because the main outflow of deep convection occurs near ~12 km, well below the tropopause level (~16 km), we investigate the large-scale vertical transport within the anticyclone. The mean vertical circulation obtained from the ERA40 reanalysis data set and a free-running general circulation model is upward across the tropopause on the eastern end of the anticyclone, as part of the balanced three-dimensional monsoon circulation. In addition to deep transport from the most intense convection, this large-scale circulation may help explain the transport of constituents to tropopause level.

## 1. Introduction

The Asian summer monsoon anticyclone is a dominant feature of the circulation in the upper troposphere – lower stratosphere (UTLS) during Northern Hemisphere (NH) summer. The anticyclone is a closed circulation, which encompasses a westerly jet in midlatitudes and an easterly jet in the tropics, and strong mean meridional motions (Dunkerton, 1995). It occurs as a response to heating associated with persistent deep convection over the South Asian region during summer (Hoskins and Rodwell, 1995; Highwood and Hoskins, 1998). The anticyclone is also observed to coincide with persistent maxima (or minima) in various trace constituents in the UTLS region, such as water vapor (Rosenlof et al., 1997; Jackson et al., 1998; Dethof et al., 1999), ozone (Randel et al., 2001; Gettelman et al., 2004), methane and nitrogen oxides (Park et al., 2004) and carbon monoxide (Filipiak et al., 2005; Li et al., 2005a; Fu et al., 2006). This likely occurs because the strong winds and closed streamlines associated with the anticyclone act to isolate air within the anticyclone (Li et al., 2005a; Randel and Park, 2006). The anticyclonic circulation and constituent extrema extend into the lower stratosphere, are an important aspect of stratosphere-troposphere coupling during summer (Dethof et al., 1999). Diagnostic and modeling studies have furthermore suggested that lower stratospheric water vapor may be strongly influenced by the upward extension of the monsoon circulation (Bannister et al., 2004; Gettelman et al., 2004; Dessler and Sherwood, 2004; Fu et al., 2006).

Recently, Randel and Park (2006, hereafter RP) have studied synoptic variability of the monsoon anticyclone and its coupling to transient deep convective forcing, as well as variability in upper tropospheric water vapor and ozone using measurements from the Atmospheric Infrared Sounder (AIRS; Aumann et al., 2003). The AIRS observations reveal coherent fluctuations in water vapor and ozone inside the anticyclone that are linked with deep convection, temperature,

1 and the intensity of the anticyclone. However, one limitation of the AIRS constituent data  
2 (particularly water vapor) is that they have an upper limit near  $\sim 150$  hPa, and they provide little  
3 quantitative information on constituents in the lower stratosphere (and their coupling to  
4 convection). The focus of this study is to analyze constituent behavior at the top of the monsoon  
5 anticyclone, using observations from the Microwave Limb Sounder (MLS) on the NASA Aura  
6 satellite (Waters et al., 2006). Aura MLS measurements include water vapor, ozone and carbon  
7 monoxide that are useful tracers of tropospheric and stratospheric air; these data have been used  
8 to document enhanced levels of carbon monoxide in the upper troposphere over the Asian  
9 monsoon (Li et al., 2005a; Filipiak et al., 2005) and also over the North American summer  
10 monsoon (Li et al., 2005b).

11       The purpose of this work is to explore constituent structure and variability in the UTLS  
12 over the Asian monsoon region based on MLS data, and study coupling to the large-scale  
13 circulation of the anticyclone and to variations in convection. Correlated variations of carbon  
14 monoxide (a tropospheric tracer) and ozone (a stratospheric tracer) are used to quantify transport  
15 behavior, and the observed coherence among deep convection, temperature and constituents are  
16 analyzed to deduce the influence of convection on the UTLS. We analyze the structure and  
17 variability of water vapor from the upper troposphere through the lower stratosphere, and  
18 quantify coherence with deep convection. A key question from the MLS data is how constituents  
19 with origins in the lower troposphere (such as carbon monoxide) attain altitudes as high as 16 km  
20 (100 hPa) as a result of convection (for which the main outflow region is closer to  $\sim 12$  km). We  
21 thus include analysis of large-scale vertical transport within the anticyclone, using three-  
22 dimensional winds from meteorological reanalyses (based on assimilation), and also on winds

from a free-running general circulation model. Idealized three-dimensional trajectory calculations are used to quantify the transport above the monsoon anticyclone.

## **2. Data and analyses**

The MLS instrument aboard the Aura spacecraft, one of the NASA Earth Observing System (EOS) platforms, has been measuring atmospheric parameters since August 2004 (Schoeberl et al., 2006). MLS uses microwave limb sounding to measure temperature and chemical constituents, including carbon monoxide (CO), water vapor (H<sub>2</sub>O) and ozone (O<sub>3</sub>) in the upper troposphere and stratosphere. The MLS field-of-view vertically scans the limb in the orbit plane and gives 82°S-82°N latitude coverage on each orbit (Waters et al., 2006). The standard MLS vertical grid has six levels per decade of pressure at  $10^{-n/6}$  hPa (...100.0, 82.5, 68.1...hPa), with a vertical resolution of ~3 km (~6 km for temperature); the available vertical coverage varies for each constituent (Livesey et al., 2005). MLS can measure in the presence of cirrus cloud and aerosol. The horizontal resolution is ~3° along the orbit, with 14 orbits per day (~25° longitude sampling).

Vertical profiles of carbon monoxide, water vapor, ozone and temperature are obtained from MLS version 1.5 (v1.5) level 2 products. We construct gridded data on 5° latitude x 10° longitude grids by averaging profiles inside the bins every two days. The quality screening of individual profiles are processed by the instructions given by Livesey et al. (2005). The single-profile precision of carbon monoxide ranges from 20 ppbv between 215-22 hPa, then increases approximately inversely with pressure (Froidevaux et al., 2006). For water vapor, typical single-profile precisions are 0.9, 0.7, and 0.5 ppmv at 215, 147, and 100 hPa, respectively (Livesey et al., 2005). The useful range of the ozone retrieval is 215 to 0.46 hPa. Within this range, MLS ozone may have a small positive bias, based on validation with ozonesondes over Beijing, China

(Bian et al., 2007). The typical estimated precision of the temperature measurement is 1 K at 100 hPa (Froidevaux et al., 2006).

We also use temperature from National Centers for Environmental Prediction/National Center for Atmospheric Research (NCEP/NCAR) reanalysis (Kalnay et al., 1996), covering the same time period as the MLS observations (summer 2005). The vertical velocity fields in NCEP data are available only over 1000-100 hPa. Because we are interested in vertical velocity fields above 100 hPa, we also include analyses of three-dimensional circulation using the ERA40 data set (Uppala et al., 2005). These data cover the period up to August 2002, so that our analyses are simply for climatological summer statistics, rather than for the specific year 2005. Outgoing longwave radiation (OLR) is used as a convective proxy and obtained from NOAA-CIRES Climate Diagnosis Center (<http://www.cdc.noaa.gov/>). These data are discussed in Liebman and Smith (1996).

We also include results on monsoon dynamical structure derived from the NCAR Community Atmosphere Model, version 3 (CAM3; Collins et al., 2006). We specifically focus on the vertical velocity fields and radiative-dynamical balance of the monsoon anticyclone in the (free-running) CAM3 results, and these are included as a complement to the results based on assimilated meteorological reanalyses. The model uses a horizontal resolution of 1° latitude x 1.25° longitude and has 26 vertical levels. We use the 2003 calendar year data extracted from a 4-year run using 2001-2004 sea surface temperatures.

### **3. Anticyclone dynamical structure and links to convection**

The climatological structure of the Asian summer monsoon anticyclone is examined using meteorological fields from NCEP reanalysis. The horizontal structure of two-month (July-August 2005) average NCEP geopotential height and wind anomalies (deviation from the zonal

mean) at 100 hPa ( $\approx 16$  km) is shown in Figure 1a. A strong anticyclonic circulation is located between  $\sim 20^\circ$ - $120^\circ$ E in NH, centered to the northwest side of the time averaged deep convection (low OLR). There is also an approximately symmetric, smaller amplitude anticyclone in the Southern Hemisphere (SH) subtropics. These anticyclonic circulations are characteristic of Rossby waves forced by low frequency heating in the tropics, and are also accompanied by a Kelvin wave signature along the equator to the east of the heating (Gill, 1980; Hoskins and Rodwell, 1995), as illustrated in Figure 1b. The fact that the convective heating is located north of the equator introduces a much stronger circulation in that hemisphere, as also discussed in Gill (1980). The schematic diagram of three-dimensional structure of this heat-induced circulation can be found in Figure 9 of Highwood and Hoskins (1998).

It is important to note the relation between the anticyclonic circulation and the location of the deep convection, as they are distinct. This is illustrated more clearly in Figure 2, which shows a streamfunction ( $\Psi$ ) highlighting the location of strongest winds at 100 hPa (used here to define the time averaged anticyclone), together with the time averaged OLR (a proxy for convection). The strongest convection occurs over the Indian Ocean and Southeast Asia, on the southeastern edge of the anticyclone; this behavior is consistent with the dynamical structure of the Gill response (Fig. 1b). There is relatively less of the deepest convection within the anticyclone, and only a weaker maximum over the Tibetan plateau (noted with grey shading in Fig. 2). Analyses of the correlations between tracers and convection (OLR) show that tracers within the anticyclone as a whole are best correlated with OLR in the region  $\sim 60^\circ$ - $120^\circ$ E and  $15^\circ$ - $30^\circ$ N, and we use OLR averaged over this area as a reference time series for the convective forcing.

1       The monsoon anticyclone is characterized by cold temperatures in the UTLS region,  
2   overlying warm anomalies in the middle troposphere (RP). Figure 3 shows the MLS time  
3   averaged (July-August) temperature at 100 hPa, expressed as deviations from the zonal mean,  
4   showing that coldest temperatures are colocated with the anticyclonic circulation (not with the  
5   strongest convection). However, temperatures within the anticyclone do vary coherently with the  
6   monsoon convection. This is illustrated in Figure 4a, showing time series of 100 hPa  
7   temperatures within the cold region (20°-40°N and 20°-120°E) together with the proxy for  
8   monsoon convection. These time series show a strong negative correlation ( $r=-0.86$ ),  
9   demonstrating that cold temperatures near the tropopause are amplified in response to the  
10   convection. The fact that the temperature response near the tropopause is not colocated with  
11   convection (Fig. 3) demonstrates that it is mainly a dynamical response, rather than a result of  
12   overshooting deep convection (e.g., Kuang and Bretherton, 2004).

13       The dynamical coupling to convection is further highlighted by examining the latitude-  
14   height structure of correlations between temperature (averaged over 20°-120°E) and the  
15   convection proxy (OLR), as shown in Figure 4b; here we use NCEP temperatures to cover a  
16   wider vertical range. The spatial patterns in Figure 4b show strong positive correlations  
17   (warming) in the troposphere and negative correlations (cooling) near and above the tropopause  
18   in the region of the anticyclone (~20°-40°N). Furthermore, there are approximately mirror-image  
19   correlation patterns in SH subtropics (~20°-35°S). This symmetric structure in the correlations is  
20   consistent with the (non-local) dynamical response to convective diabatic heating discussed  
21   above (Fig. 1). Overall, both the time average structure of temperature (Fig. 3) and space-time  
22   coherence with convection (Figs. 4a-b) demonstrate that non-local convection primarily controls  
23   temperature variability within the anticyclone.



#### 4. Carbon monoxide and ozone

The climatological behavior of tracers in the UTLS is closely linked to the dynamical structure seen in Figure 1. The horizontal structure of July-August 2005 average carbon monoxide and ozone at 100 hPa is shown in Figure 5. Carbon monoxide has a broad maximum within the Asian monsoon anticyclone, which is defined as a streamfunction contour, over 20°-120°E in the NH subtropics. These relatively high values of carbon monoxide near the tropopause are evidence of transport from near-surface levels (Filipiak et al., 2005; Li et al., 2005a). MLS ozone exhibits a minimum over the same region, colocated with the maximum in carbon monoxide. This structure is consistent with the minimum in upper tropospheric ozone observed from AIRS data (Fig. 1 of RP), and likely results from the upward transport of near-surface air with low ozone mixing ratios.

There is a substantially weaker anticyclone apparent over North America in Figure 1a, and little evidence of corresponding carbon monoxide or ozone extrema in Figure 5. However, a weak secondary maximum in carbon monoxide is present over the SH subtropics in the longitude band of the Asian monsoon. There is a similar structure for (low) ozone, with the minimum in SH subtropics having relatively lower values with a broad zonal structure (~60°-180°E). The overall ozone structure in Figure 5b is consistent with the climatology from the Stratospheric Aerosol and Gas Experiment (SAGE) II measurements (Fig. 7(b) of Randel et al., 2001).

The meridional structure of July-August 2005 averaged carbon monoxide for 20°-100°E longitudes (over the monsoon region) is shown in Figure 6. Due to known biases in the data in the tropics, we only show results above 215 hPa. Isentropes are added as thin solid lines in Figure 6, and the thermal tropopause is marked as a thick dashed line. There is evidence of increased carbon monoxide above the tropopause in both hemispheres (around 30° latitude), and

1 these correspond to the maxima observed over the Asian monsoon and in the SH subtropics (and  
2 minima near the equator) in Figure 5a. This ‘double-peak’ structure is most evident from the  
3 tropopause up to 68 hPa, and is also seen in other MLS tracers such as water vapor, HCl and  
4 HNO<sub>3</sub> (not shown).

5 The synoptic variability of carbon monoxide and ozone at 100 hPa in the region of the  
6 anticyclone throughout the summer is shown via Hovmöller diagrams in Figure 7. Relatively  
7 high CO mixing ratios are observed in the monsoon region (~20°-120°E), with a clear maximum  
8 in June, and several slightly smaller maxima in July and August. Variability observed in CO is  
9 closely coupled to that of ozone in Figure 7b, with high CO linked with low ozone. The episodic  
10 highest values of CO and lowest ozone are observed over longitudes ~60°-100°E, and  
11 subsequently move westward, which likely results from advection by the anticyclonic flow  
12 (easterly winds in the latitude band 10°-30°N). This strong anticorrelation between carbon  
13 monoxide and ozone demonstrates a common source of variability within the Asian monsoon  
14 anticyclone at this level, and this coupling is enhanced by dynamical confinement within the  
15 anticyclone (Li et al. 2005a; RP).

16 Figure 8 compares time series of 100 hPa carbon monoxide inside the anticyclone with  
17 the OLR convection proxy from May to September 2005. Carbon monoxide is averaged over  
18 15°-30°N and 20°-100°E at 100 hPa, where the climatology shows a maximum in Figure 5a.  
19 Figure 8 shows a strong correlation ( $r=0.77$ ) between variations in deep convection and carbon  
20 monoxide without evidence of substantial time lags. This relationship is similar to that found  
21 between deep convection and upper tropospheric water vapor in the monsoon region, as shown  
22 in RP. There is a corresponding negative correlation between ozone at 100 hPa and the  
23 convection proxy time series (not shown).

Because CO and ozone act as tracers of tropospheric and stratospheric air, respectively, their statistical relationship can be used to quantify air mass characteristics and origins. Several studies have used tracer-tracer relationships between constituents with tropospheric and stratospheric sources (particularly CO and ozone) to identify the transition region between troposphere and stratosphere air masses (Fischer et al., 2000; Hoor et al., 2002; Pan et al., 2004). The co-variability of CO and ozone at 100 hPa over 60°S-60°N for 1-5 July is shown as a scatter plot in Figure 9a. While the overall pattern in Figure 9a is similar to that observed in aircraft measurements (e.g., Fischer et al., 2000), the relationships are less compact, and it is not simple to empirically define stratospheric and tropospheric air masses in the MLS data. This is possibly due to the vertical resolution and limb path averaging associated with the MLS observations, and possibly noise in the respective retrievals. Instead of fitting linear slopes to identify stratospheric and tropospheric air masses as used in Pan et al. (2004), we empirically choose specific values of carbon monoxide and ozone to identify air mass characteristics. Accordingly, we define stratospheric air as containing high ozone ( $\geq 300$  ppbv) and low carbon monoxide ( $< 60$  ppbv), and tropospheric air as having low ozone ( $< 300$  ppbv) and high carbon monoxide ( $\geq 60$  ppbv). Air with characteristics midway between these limits is then specified as a transition region (blue dots in Fig. 9a).

Using this CO-ozone relationship, we use each MLS profile measurement over two months to quantify statistical characteristics of air masses at 100 hPa, and present a map in Figure 9b. First, we assign three primary colors (red, yellow and blue) to each point according to the relationship in Figure 9a on a profile-by-profile basis. Then, measurements are accumulated for July and August and binned in  $2.5^\circ$  latitude  $\times$   $5^\circ$  longitude grid boxes (with typically 20-40 observations in each box). The colors in the map (Fig. 9b) are then determined by the relative

numbers of air types accumulated in the grid boxes, and this shows the statistical characteristics of air in the individual measurements over two months. The primary color is given where the largest number is bigger than twice the second number, and the statistical properties of the transition regions are further separated by using mixed colors (e.g., green=yellow+blue, purple=red+blue, and orange=red+yellow). For example, green denotes an approximately equal mixture of stratosphere (yellow) and transition region (blue) air. The results in Figure 9b show that air within the monsoon anticyclone has a primarily tropospheric signature (red points, representing high carbon monoxide and low ozone). Air throughout the rest of the tropics has mixed characteristics, with a transition to stratospheric air at higher latitudes. More frequent transitions between the stratosphere and transition region (green points) occur on the eastern side of the Asian anticyclone and also near North America in Figure 9b; these are regions of frequent troposphere-stratosphere transport (Stohl et al., 2003) and Rossby wave breaking (Postel and Hitchmann, 1999) during NH summer. Also, there are a few orange points denoting approximately equal proportions of stratospheric and tropospheric air (but less transition air) on the northern edge of the Asian anticyclone. A corresponding analysis at 68 hPa (not shown) suggests that tropospheric or transition air exists in the Asian summer monsoon region and the SH subtropics, while air over the rest of the globe is stratospheric in character. The overall results are not sensitive to the exact threshold values chosen above.

## **5. Water vapor**

Relatively high values of water vapor near the tropopause are a well-known observational feature of the Asian monsoon anticyclone (e.g., Rosenlof et al., 1997; Randel et al., 2001; Dessler and Sherwood, 2004; Gettelman et al., 2004). Calculated relative humidity values in this region are high, and frequent subvisual cirrus clouds are a climatological feature near the

1 tropopause (Wang et al., 1996; Massie et al., 2002). However, the processes maintain high water  
2 vapor in this region are poorly understood, including the specific links to variability in lower  
3 altitudes, convection and clouds. Here we analyze the behavior of MLS water vapor, and  
4 describe the space-time variability in relation to these factors (although the MLS data do not  
5 include information regarding tropopause cirrus clouds).

6       The horizontal structures of July-August 2005 average water vapor in the upper  
7 troposphere (216 hPa) and near the tropopause (100 hPa) are shown in Figure 10; note there is  
8 more than an order of magnitude difference in the amount of water vapor at these levels. The  
9 water vapor at 216 hPa (Fig. 10b) shows a maximum that is nearly coincident with the region of  
10 deep convection on the southeast side of the anticyclone. The time average structure at 100 hPa  
11 (Fig. 10a) shows a contrasting spatial structure, with highest water vapor centered within the  
12 anticyclone (similar to CO and ozone) and distant from the deepest convection. Figure 11 shows  
13 time series of the water vapor mixing ratio at these two pressure levels (averaged over the  
14 respective maxima, 40°-100°E at 100 hPa and 60°-120°E at 216 hPa, respectively) together with  
15 the reference OLR time series. The water vapor at 216 hPa shows strong correlation with OLR  
16 ( $R=0.86$ ), demonstrating that water vapor in the upper troposphere is coherent with monsoon deep  
17 convection both temporally and spatially. This finding is consistent with the results of RP based  
18 on AIRS data, and can be reasonably explained as simple upward transport of water vapor within  
19 deep convection.

20       The time variability of water vapor at 100 hPa in Figure 11(top) shows less correlation  
21 ( $R=0.6$ ) with OLR than data at lower levels. This in addition to the 100 hPa water vapor  
22 maximum being spatially removed from the deep convection (Fig. 10a) suggests more  
23 complicated behavior than simple vertical transport to this level. Time series of relative humidity

1 derived from MLS data in this region at 100 hPa show relatively high values (~60-100%), with  
2 variability primarily linked to temperatures within the anticyclone (not shown). The high relative  
3 humidity, together with the climatological occurrence of tropopause cirrus clouds noted above,  
4 suggest that in situ dehydration could contribute to the decoupling of water vapor at 100 hPa  
5 with values below (although dehydration is difficult to diagnose based on the area averages  
6 inherent to satellite data, together with a lack of synoptic cirrus observations). It is also possible  
7 that overshooting deep convection could directly influence the water vapor budget at this level,  
8 at scales smaller than those observed by MLS. However, the results of Gettelman et al. (2002)  
9 show that almost no convection reaches to the tropopause level in this region (over Iran and  
10 Afghanistan).

## 11 **6. Large-scale vertical transport in the monsoon anticyclone**

12 The observations of MLS carbon monoxide and ozone show clear evidence of  
13 tropospheric air at altitudes near (and above) the tropopause within the anticyclone, and a natural  
14 question is how these tracers reach such high altitudes (> 16 km). It is likely that deep convection  
15 is responsible for transporting near-surface air vertically into the middle and upper troposphere,  
16 but the outflow level for the majority of deep convection is probably near or below ~12 km, with  
17 a small fraction reaching the tropopause level (Gettelman et al., 2002; Liu and Zipser, 2005).  
18 While this small fraction could still significantly influence the budgets of CO, ozone and water  
19 vapor near the tropopause (Dessler, 2002; Dessler and Sherwood, 2004), it is also of interest to  
20 understand the large-scale vertical circulation in the anticyclone.

21 It is straightforward to analyze vertical transport based on vertical velocities derived from  
22 operational or reanalysis data sets. However, there are substantial uncertainties in vertical  
23 velocities in the UTLS region in current assimilated data sets, because the values are relatively

small (derived as a result of assimilated horizontal wind and temperature fields) and there are no direct measurements of vertical velocity that contribute to the assimilation. Thus the vertical velocities in analyses or reanalyses are not well constrained and may reflect the behavior (biases) of the underlying assimilation model, and should be interpreted in that light. Therefore we have analyzed results from two sources: we use ‘observational’ data from the ERA40 reanalysis data set, covering the years 2000-2002, and we also include results from a free running climate model (CAM3, Collins et al., 2006). The CAM3 results are complementary to the ERA40 assimilation data in that they are not influenced by assimilation of sparse data over the UTLS monsoon region.

Figure 12a shows a horizontal map of the July-August average vertical velocity at 104 hPa derived from the ERA40 reanalysis data (averaged over 2000-2002), together with the 214 hPa horizontal wind vectors and a few geopotential height contours at 200 hPa for the same period (which highlight the location of the Asian monsoon anticyclone). The ERA40 vertical velocity shows upward motion over the eastern side of the anticyclone, with magnitude  $\sim 0.6$  mm sec<sup>-1</sup>, and weak ( $\sim 0.2$  mm sec<sup>-1</sup>) downward motion over the western side. There is also upward vertical velocity in the SH subtropics near the region of the weaker, symmetric anticyclone  $\sim 20^\circ$ S (Fig. 1a), but relatively weak upwelling over the equator (aside from a localized region near the date line). A vertical cross-section of the ERA40 vertical velocity over longitudes  $60^\circ$ - $150^\circ$ E (the region of maximum values) is shown in Figure 12b. This reveals strong upward vertical velocity throughout the troposphere (the rising branch of the Hadley circulation, associated with persistent deep convection), and this upward motion extends across the tropopause into the lower stratosphere. There is also a region of upward motion in the SH subtropics ( $\sim 20^\circ$ S), near and above the tropopause.

Corresponding results from the CAM3 simulation show very similar results. CAM3 reproduces a reasonable Asian summer monsoon anticyclonic circulation, and the near-tropopause vertical velocity in the model exhibits structure very similar to the ERA40 results. The model exhibits strongest upward motion over the eastern half of the anticyclone, minimum vertical velocity over the equator, and a secondary maximum in the SH subtropics. Figure 13a shows a vertical cross section of the CAM3 vertical velocity sampled identically to the ERA40 results in Figure 12b, showing similar upward motion across the tropopause in both the NH and SH subtropics. The fact that the free-running climate model produces vertical velocity patterns that are similar to the reanalysis is encouraging that this is a robust dynamical feature of the monsoon circulation in the UTLS region.

The CAM3 results allow further study of the dynamic and thermodynamic balances leading to the calculated upward velocities. Figure 13b shows the net radiative heating rates derived from the model, sampled identically to the vertical velocity field in Figure 13a. The results show positive radiative heating in the regions of upward velocity in the UTLS region, on top of the Asian monsoon anticyclone, and also in the SH subtropics. This positive radiative heating (from longwave radiation) occurs as response to the anomalously cold temperatures near and above the tropopause, which in turn exist as part of the upward circulation in this region (hence the similarity between upward velocity and positive radiative heating in Fig. 13). The symmetric spatial structure suggests that the temperature patterns and upward motion in the anticyclone are part of the three-dimensional balanced dynamical structure of the circulation seen in Fig. 1 (i.e., part of the response to convective heating centered near the equator, see also Highwood and Hoskins, 1998). We note that the weak upward circulation in the SH subtropics in Figs. 12-13 is consistent with the small maximum in CO in this region (Fig. 5a), and the overall



1 symmetric patterns in upwelling are consistent with the double-peaked structure observed in CO  
2 near the tropopause in the monsoon region (Fig. 6).

3 A more quantitative estimate of the contribution of resolved (large-scale) upwelling to  
4 transport in the anticyclone can be derived from three-dimensional trajectory calculations  
5 (Bowman, 1993). We have made some preliminary estimates based on ERA40 winds (figures are  
6 not included here). We assume an idealized distribution of parcels initialized inside the  
7 anticyclone in the upper troposphere, hypothetically resulting from the outflow of deep  
8 convection (beginning on the 200-150 hPa levels). The trajectory results show relatively rapid  
9 vertical spreading of the particles both upward and downward over a distance of several km after  
10 only a few days; it is unclear if this is realistic, or the result of excess noise in the ERA40 vertical  
11 velocity fields. The majority of particles remain inside the anticyclone for a period of several  
12 weeks, consistent with the results of RP (see Figs. 13-14 of RP). During this time the altitude of  
13 the ensemble average rises only very slowly (a net of  $\sim 0.5$  km over 14 days), and in fact the  
14 vertical dispersion (noted above) appears more effective at moving particles upwards than the  
15 mean circulation alone. Overall these calculations suggest that the large-scale circulation is  
16 capable of moving some fraction of air detrained from deep convection to the near-tropopause  
17 level with a time scale of a few days, although these are highly simplified and idealized estimates,  
18 and further analysis is warranted.

## 19 **7. Summary and discussion**

20 The Asian summer monsoon anticyclone is the dominant circulation feature in the UTLS  
21 during NH summer. The anticyclone is a thermally driven circulation forced by persistent deep  
22 convection over India and the Bay of Bengal during summer. The dynamical structure of the  
23 circulation (including the symmetric anticyclone in the SH subtropics) is consistent with the

1 idealized calculations of Gill (1980), and also the more realistic model of Hoskins and Rodwell  
2 (1995). The results show that heating centered north of the equator results in symmetric  
3 anticyclonic circulation systems, with stronger response in the NH. The strong coherence  
4 between transient convection and remote temperature fluctuations (Fig. 4) is convincing  
5 evidence of these dynamical links. The cold temperatures near the tropopause are a result of the  
6 large-scale balanced dynamics, not a result of convective overshooting (as the cold temperatures  
7 are not colocated with convection; see Fig. 3). The OLR data show that the strongest convection  
8 occurs to the south-east of the anticyclone, not over the Tibet plateau (Fig. 2); this result is  
9 somewhat different to the analyses of Fu et al. (2006), who argue for a dominant role of  
10 convection over the Tibet plateau region.

11         The strong winds of the Asian summer monsoon anticyclone act to isolate air from the  
12 surrounding area, with the result that tracer observations often show extrema within the  
13 anticyclone throughout the UTLS (Park et al., 2004; Li et al., 2005a; RP). The MLS observations  
14 here show that this behavior extends into the lower stratosphere, with maxima in carbon  
15 monoxide and water vapor, and minima in ozone, on top of the Asian monsoon anticyclone.  
16 There are also smaller magnitude constituent maxima in the SH subtropics, near the  
17 corresponding SH anticyclone, so that there is a double-peaked latitudinal structure over the  
18 longitude range  $\sim 20^{\circ}$ - $120^{\circ}$ E. The high carbon monoxide and low ozone signatures near the  
19 tropopause suggest that air in these regions is mostly tropospheric in character. The MLS  
20 observations furthermore show that variations in carbon monoxide (and ozone) at 100 hPa within  
21 the anticyclone are coupled to the monsoon deep convection (Figs. 7-8). Overall, the  
22 observations are consistent with the vertical transport of lower tropospheric air to the UTLS  
23 region (linked with deep convection), and confinement within the anticyclone.

1        We have used CO-ozone correlations derived from the MLS data to empirically  
2        characterize air with stratospheric and tropospheric character, and transitional behavior. The  
3        MLS data show the characteristic ‘L-shaped’ structure to the CO-ozone correlations (Fig. 9a),  
4        although the relationships are less compact than those derived from high-resolution aircraft  
5        measurements (e.g., Hoor et al., 2002; Pan et al., 2004); this may be a result of the limb path  
6        averaging inherent to the MLS data, or possibly noise in the individual retrievals. In any case,  
7        these correlations allow statistical characterization of regions of stratospheric and tropospheric  
8        air, and locations that contain some mixture of the two (Fig. 9b). According to this diagnostic the  
9        eastern edge of the monsoon anticyclone has a relatively high frequency of transition region air,  
10       and thus might be regions of more frequent stratosphere-troposphere exchange.

11       Upper tropospheric water vapor in the monsoon region is strongly coherent with deep  
12       convection, both spatially and temporally. However, at the altitude of the tropopause, maximum  
13       water vapor is centered within the anticyclone (similar to CO), distant from the deepest  
14       convection; it is also less temporally correlated with convective intensity. It is likely that the  
15       processes that transport (high) CO and (low) ozone to 100 hPa within the anticyclone also  
16       transport relatively high water vapor, and so the lack of strong correlation between convection  
17       and water vapor at 100 hPa might suggest additional processes acting on water vapor (namely,  
18       dehydration and/or direct transport within overshooting convection). Calculation of the relative  
19       humidity at 100 hPa from the MLS data shows relatively high values (~60-100%), and  
20       variability is mainly controlled by temperature. One possibility is that the cold tropopause  
21       temperatures lead to frequent dehydration, and this contributes to decoupling water vapor and the  
22       other tracers (and frequent formation of cirrus cloud near the tropopause). However, the large  
23       volume sampling of MLS data (which precludes estimates of local supersaturation), plus the lack

1 of synoptic information on cirrus clouds near the tropopause do not allow quantitative  
2 assessment of this mechanism at present.

3       The MLS data suggest that air near the tropopause (~16 km) has been transported from  
4 the lower troposphere and is linked to deep convection, although a relatively small fraction of  
5 convection detrains above 12 km. While a small amount of overshooting convection can  
6 contribute significantly to chemical budgets (Dessler and Sherwood, 2004), we have also  
7 investigated the large-scale vertical transport in the anticyclone. We have analyzed the vertical  
8 velocities from ERA40 reanalysis (with assimilated observations) and a free-running climate  
9 model (CAM3) in the UTLS region. Both data sources show slow upward motion across the  
10 tropopause, with a maximum over the eastern side of the Asian anticyclone (Fig. 12); there is  
11 also a weaker maximum associated with the anticyclone over the SH subtropics. This upward  
12 circulation is in balance with anomalously cold temperatures near the tropopause, which results  
13 in positive longwave radiative heating (diagnosed with the CAM3 results). The upward  
14 circulation in the anticyclone is consistent with enhanced carbon monoxide mixing ratios  
15 crossing the tropopause. A weaker maxima in carbon monoxide above the tropopause, and weak  
16 upward motion, is also observed in the SH subtropics (far removed from deep convection). This  
17 symmetric pattern of upward circulation is in quantitative agreement with the double-peaked  
18 meridional structure observed in CO near the tropopause (Fig. 6). Quantitative estimates of  
19 vertical transport based on three-dimensional trajectory calculations using the ERA40 winds  
20 show slow upward net transport of particles within the anticyclone, in addition to rapid vertical  
21 dispersion (which may or may not be a realistic result). There are substantial uncertainties in  
22 these calculations, so that the details of large-scale vertical transport (and the contribution of  
23 overshooting convection) are topics that require more investigation.

1  
2  
3  
4  
5  
6  
7  
8  
9  
10  
11

**Acknowledgements**

The National Center for Atmospheric Research is operated by the University Corporation for Atmospheric Research, under sponsorship of the National Science Foundation. This work was partially supported under the NASA ACMAP Aura Validation Project. We thank three anonymous reviewers for detailed and thoughtful reviews, which resulted in substantial improvements to an earlier version of this paper. We thank the MLS instrument team for discussions and production of an excellent data product. We thank Phil Duffy of Lawrence Livermore National Labs for assisting with the CAM runs.

## References

- Aumann, H. H., et al. (2003), AIRS/AMSU/HSB on the Aqua Mission: Design, science objectives and data products, *IEEE Trans. Geosci. Remote Sens.*, *41*, 253-264.
- Bannister, R. N., A. O'Neill, A. R. Gregory, and K. M. Nissen (2004), The role of the south-east Asian monsoon and other seasonal features in creating the 'tape-recorder' signal in the Unified Model, *Q. J. R. Meteorol. Soc.*, *130*, 1531-1554.
- Bian, J., A. Gettelman, H. Chen, and L. L. Pan (2007), Validation of satellite ozone profile retrievals using Beijing ozonesonde data, *J. Geophys. Res.*, *112*, D06305, doi:10.1029/2006JD007502.
- Bowman, K. P. (1993), Large-scale isentropic mixing properties of the Antarctic polar vortex from analyzed winds, *J. Geophys. Res.*, *98*, 23,013-23,027.
- Collins, W. D., et al. (2006), The formulation and atmospheric simulation of the Community Atmosphere Model version 3 (CAM3), *J. Clim.*, *19*, 2144-2161.
- Dessler, A.E. (2002), The effect of deep tropical convection on the tropical tropopause layer. *J. Geophys. Res.*, *107*, D34033, doi:10.1029/2001JD000511.
- Dessler, A. E., and S. C. Sherwood (2004), Effect of convection on the summertime extratropical lower stratosphere. *J. Geophys. Res.*, *109*, doi:10.1029/2004JD005209.
- Dethof, A., A. O'Neill, J. M. Slingo, and H. G. J. Smit (1999), A mechanism for moistening the lower stratosphere involving the Asian summer monsoon, *Q. J. R. Meteorol. Soc.*, *125*, 1079-1106.
- Dima, I. M., J. M. Wallace, and I. Kraucunas (2005), Tropical Zonal Momentum Balance in the NCEP Reanalyses. *J. Atmos. Sci.*, *62*, 2499-2513.
- Dunkerton, T. J. (1995), Evidence of meridional motion in the summer lower stratosphere adjacent to monsoon regions, *J. Geophys. Res.*, *100(D8)*, 16,675-16,688.
- Efron, B., and R. J. Tibshirani (1993), *An Introduction to the Bootstrap*, 436 pp., CRC Press, Boca Raton, Fla.
- Filipiak, M. J., R. S. Harwood, J. H. Jiang, Q. Li, N. J. Livesey, G. L. Manney, W. G. Read, M. J. Schwartz, J. W. Waters, and D. L. Wu (2005), Carbon monoxide measured by the EOS Microwave Limb Sounder on Aura: First results, *Geophys. Res. Lett.*, *32*, L14825, doi:10.1029/2005GL022765.
- Fischer, H., F. G. Wienhold, P. Hoor, O. Bujok, C. Schiller, P. Siegmund, M. Ambaum, H. A.

- 1 Scheeren, and J. Lelieveld (2000), Tracer correlations in the northern high latitude  
2 lowermost stratosphere: Influence of cross-tropopause mass exchange, *Geophys. Res. Lett.*,  
3 27, 97–100.
- 4 Froidevaux, L. et al. (2006), Early validation analyses of atmospheric profiles 1 from EOS MLS  
5 on the Aura satellite, *IEEE Trans. Geosci. Remote Sens.*, 44(5), 1106–1121.
- 6 Fu, R., Y. Hu, J. S. Wright, J. H. Jiang, R. E. Dickinson, M. Chen, M. Filipiak, W. G. Read, J. W.  
7 Waters, and D. L. Wu (2006), Short circuit of water vapor and polluted air to the global  
8 stratosphere by convective transport over the Tibetan Plateau, *PNAS*, 103, 5664–5669.
- 9 Gettelman, A., M. L. Salby, and F. Sassi (2002), Distribution and influence of convection in the  
10 tropical tropopause region, *J. Geophys. Res.*, 107(D10), 4080, doi:10.1029/2001JD001048.
- 11 Gettelman, A., D. E. Kinnison, T. J. Dunkerton, and G. P. Brasseur (2004), Impact of monsoon  
12 circulations on the upper troposphere and lower stratosphere, *J. Geophys. Res.*, 109,  
13 D22101, doi:10.1029/2004JD004878.
- 14 Gill, A.E. (1980), Some simple solutions for heat-induced tropical circulation. *Q. J. R. Meteorol.*  
15 *Soc.*, 106, 447–462.
- 16 Highwood, E. J., and B. J. Hoskins (1998), The tropical tropopause, *Q. J. R. Meteorol. Soc.*, 124,  
17 1579–1604.
- 18 Hoor, P., H. Fischer, L. Lange, J. Lelieveld, and D. Brunner (2002), Seasonal variations of a  
19 mixing layer in the lowermost stratosphere as identified by the CO-O<sub>3</sub> correlation from in  
20 situ measurements, *J. Geophys. Res.*, 107(D5), doi:10.1029/2000JD000289.
- 21 Hoskins, B. J., and M. J. Rodwell (1995), A model of the Asian summer monsoon. Part I: The  
22 global scale, *J. Atmos. Sci.*, 52, 1329–1340.
- 23 Jackson, D. R., S. J. Driscoll, E. J. Highwood, J. E. Harries, and J. M. Russell III (1998),  
24 Troposphere to stratosphere transport at low latitudes as studied using HALOE  
25 observations of water vapour 1992–1997, *Q. J. R. Meteorol. Soc.*, 124, 169–192.
- 26 Jensen, E. J., W. G. Read, J. Mergenthaler, B. J. Sandor, L. P. Ster, and A. Tabazadeh (1999),  
27 High humidities and subvisible cirrus near the tropical tropopause, *Geophys. Res. Lett.*, 26,  
28 2347–2350.
- 29 Kalnay, E., et al. (1996), The NCEP/NCAR 40-year reanalysis project, *Bull. Am. Meteorol. Soc.*,  
30 77, 437–471.
- 31 Kuang, Z., and C. S. Bretherton (2004), Convective influence on the heat balance of the tropical

1 tropopause layer: A cloud-resolving model study, *J. Atmos. Sci.*, 61, 2919-2927.

2 Li, Q., et al. (2005a), Trapping of Asian pollution by the Tibetan anticyclone: A global CTM  
3 simulation compared with EOS MLS observations, *Geophys. Res. Lett.*, 32, L14826,  
4 doi:10.1029/2005GL022762.

5 Li, Q., et al. (2005b), North American pollution outflow and the trapping of convectively lifted  
6 pollution by upper-level anticyclone, *J. Geophys. Res.*, 110, D10301  
7 doi:10.1029/2004JD005039.

8 Liebman, B., and C.A. Smith (1996), Description of a complete (interpolated) outgoing  
9 longwave radiation dataset. *Bull. Am. Meteorol. Soc.*, 77, 1275-1277.

10 Liu, C., and E. J. Zipser (2005), Global distribution of convection penetrating the tropical  
11 tropopause, *J. Geophys. Res.*, 110, D23104, doi:10.1029/2005JD006063.

12 Livesey, N. J., et al. (2005), "Data Quality Document for the EOS MLS Version 1.5 Level 2  
13 Data Set," distributed with MLS data by the GES DAAC and available at  
14 <http://mls.jpl.nasa.gov>.

15 Massie, S., A. Gettelman, W. Randel, and D. Baumgardner (2002), Distribution of tropical cirrus  
16 in relation to convection, *J. Geophys. Res.*, 107(D21), 4591, doi:10.1029/2001JD001293.

17 Mote, P. W., et al. (1996), An atmospheric tape recorder: The imprint of tropical tropopause  
18 temperatures on stratospheric water vapor, *J. Geophys. Res.*, 101(D2), 3989-4006.

19 Pan, L. L., W. J. Randel, B. L. Gary, M. J. Mahoney, and E. J. Hints (2004), Definitions and  
20 sharpness of the extratropical tropopause: A trace gas perspective, *J. Geophys. Res.*, 109,  
21 D23103, doi:10.1029/2004JD004982.

22 Park, M., W. J. Randel, D. E. Kinnison, R. R. Garcia, and W. Choi (2004), Seasonal variation of  
23 methane, water vapor, and nitrogen oxides near the tropopause: Satellite observations and  
24 model simulations, *J. Geophys. Res.*, 109, D03302, doi:10.1029/2003JD003706.

25 Postel, G. A., and M. H. Hitchman (1999), A climatology of Rossby waves breaking along the  
26 subtropical tropopause. *J. Atmos. Sci.*, 56, 359-373.

27 Randel, W. J., F. Wu, A. Gettelman, J. M. Russell III, J. M. Jawodny, and S. J. Oltmans (2001),  
28 Seasonal variation of water vapor in the lower stratosphere observed in Halogen  
29 Occultation Experiment data, *J. Geophys. Res.*, 106, 14,313-14,325.

30 Randel, W. J., and M. Park (2006), Deep convective influence on the Asian summer monsoon  
31 anticyclone and associated tracer variability observed with Atmospheric Infrared Sounder



(AIRS), *J. Geophys. Res.*, *111*, D12314, doi:10.1029/2005JD006490.

Rosenlof, K. H., A. F. Tuck, K. K. Kelly, J. M. Russell III, and M. P. McCormick (1997), Hemispheric asymmetries in water vapor and inferences about transport in the lower stratosphere, *J. Geophys. Res.*, *102*, 13,213-13,234.

Schoeberl, M. R., et al. (2006), Overview of the EOS aura mission, *IEEE Trans. Geosci. Remote Sens.*, *44*(5), 1066-1074.

Stohl, A., H. Wernli, P. James, M. Bourqui, C. Forster, M. A. Liniger, P. Seibert, and M. Sprenger (2003), A new perspective of stratosphere-troposphere exchange, *Bull. Am. Met. Soc.*, *84*, 1565–1573.

Uppala, S.M. et al. (2005), The ERA-40 re-analysis, *Q. J. R. Meteorol. Soc.*, *131*, 2691-3012.

Wang, P. -H., P. Minnis, M. P. McCormick, G. S. Kent, and K. M. Skeens (1996), A 6-year climatology of cloud occurrence frequency from Stratospheric Aerosol and Gas Experiment II observations (1985 - 1990), *J. Geophys. Res.*, *101*, 29,407-29,430.

Waters, J. W., et al. (2006), The Earth Observing System Microwave Limb Sounder (EOS MLS) on the Aura satellite, *IEEE Trans. Geosci. Remote Sens.*, *44*(5), 1075–1092.

## Figure Captions

Figure 1. (a) Horizontal structures of July-August 2005 average NCEP geopotential height anomalies (deviations from the zonal mean, unit: meter) and horizontal winds ( $\text{m s}^{-1}$ ) at 100 hPa. Horizontal wind fields are shown as vectors and shaded regions indicate deep convection ( $\text{OLR} \leq 205 \text{ W m}^{-2}$ ). (b) Revised 'Gill-type' solution at the upper level of the atmosphere (adapted from Fig. 1b of Gill, 1980). Shaded regions indicate the imposed heat source.

Figure 2. Climatological location of the monsoon anticyclone (defined as streamfunction ( $\Psi$ ) calculated from NCEP horizontal winds, contour:  $400 \text{ m}^2 \text{ s}^{-1}$ ) averaged in July-August 2005. Red contours indicate deep convection ( $\text{OLR}$  contours of 205, 195, 185...  $\text{W m}^{-2}$ , with values below 195 hatched red) and Tibetan plateau is shown as grey shading where the elevation is  $\geq 3\text{km}$ .

Figure 3. Horizontal structure of July-August 2005 average temperature anomaly (deviations from the zonal mean, unit: K) at 100 hPa. Overlaid is a streamfunction ( $\Psi$ ) contour ( $400 \text{ m}^2 \text{ s}^{-1}$ ) defining the monsoon anticyclone, from Fig. 2.

Figure 4. (a)  $\text{OLR}$  ( $\text{W m}^{-2}$ ) time series averaged in  $15^\circ\text{-}30^\circ\text{N}$  and  $60^\circ\text{-}120^\circ\text{E}$  longitudes (plus) and MLS temperature (K) time series at 100 hPa averaged in  $15^\circ\text{-}30^\circ\text{N}$  and  $20^\circ\text{-}120^\circ\text{E}$  longitudes (solid) from May to September 2005. Correlation coefficient ( $r=-0.86$ ) is noted at the upper right. (b) Correlations between the  $\text{OLR}$  time series averaged over  $15^\circ\text{-}30^\circ\text{N}$  and  $60^\circ\text{-}120^\circ\text{E}$  and the NCEP temperature anomaly (deviations from the zonal mean) averaged over  $20^\circ\text{-}120^\circ\text{E}$  for May to September 2005. Contour interval is 0.25 and zero contour is omitted. Plus and minus signs indicate the strongest correlations in both hemispheres. The 5% significance level, evaluated using a resampling technique (Efron and Tibshirani, 1993), is near 0.3 and shown as shadings. Thermal tropopause derived from NCEP/NCAR reanalysis is noted by thick solid line and the topography is added at the bottom.

Figure 5. Horizontal structures of July-August 2005 average (a) MLS carbon monoxide (ppbv) and (b) ozone (ppbv) at 100 hPa. Thick dashed lines indicate the  $400 \text{ m}^2 \text{ s}^{-1}$  streamfunction ( $\Psi$ ) contour defining the monsoon anticyclone (as in Fig. 2).

Figure 6. Vertical structures of July-August 2005 average MLS carbon monoxide (ppbv) averaged over  $20^\circ\text{-}100^\circ\text{E}$ . Thin solid lines denote isentropes (320, 340, 360, 380, 450

and 500 K) and thermal tropopause derived from NCEP/NCAR reanalysis is noted by thick dashed line.

Figure 7. Hovmöller diagrams of (a) MLS carbon monoxide (ppbv) and (b) ozone (ppbv) at 100 hPa averaged over 15°-30°N from June to August 2005.

Figure 8. (bottom) OLR ( $\text{W m}^{-2}$ ) time series averaged over 15°-30°N and 60°-120°E. (top) MLS carbon monoxide (ppbv) time series at 100 hPa averaged over 15°-30°N and 20°-100°E from May to September 2005. Correlation coefficient ( $r=0.77$ ) is noted at the upper right.

Figure 9. (a) Scatter plot of MLS carbon monoxide (ppbv) and ozone (ppbv) at 100 hPa over 60°S-60°N for 1-5 July 2005. The yellow dots represent stratospheric air ( $\text{O}_3 \geq 300$  and  $\text{CO} < 60$  ppbv) and the red dots denote tropospheric air ( $\text{O}_3 < 300$  and  $\text{CO} \geq 60$  ppbv), respectively. The blue dots located in between denote the troposphere and stratosphere transition layer. (b) Map of air mass statistics diagnosed from CO- $\text{O}_3$  relationship in Figure 9(a) for July-August 2005. Colors represent statistical air mass characteristics defined in this study, e.g., yellow – stratosphere, red – troposphere, blue – transition layer, green – stratosphere or transition layer, purple – troposphere or transition layer, orange – stratosphere or troposphere. See text for details.

Figure 10. Horizontal structures of July-August 2005 average (a) MLS water vapor (ppmv) at 100 hPa and (b) 216 hPa. Solid lines indicate deep convection, with contours as in Fig. 2. Thick dashed lines indicate (a) 400 and (b) 730  $\text{m}^2 \text{s}^{-1}$  streamfunction contours defining the monsoon anticyclone, respectively.

Figure 11. (bottom) OLR ( $\text{W m}^{-2}$ ) and MLS 216 hPa water vapor (ppmv) time series averaged over 15°-30°N and 60°-120°E. The correlation coefficient ( $R=0.86$ ) is shown at the bottom. (top) MLS water vapor (ppmv) time series averaged over 15°-30°N and 40°-100°E at 100 hPa for May to September 2005.

Figure 12. (a) Horizontal map of July-August average ERA40 vertical velocity ( $\text{mm s}^{-1}$ ) averaged for 2000-2002 at 104 hPa (averaged 95 and 113 hPa). Red and blue shaded regions indicate upward and downward vertical velocity, respectively. A number of geopotential height contours at 200 hPa are overlaid to identify the Asian anticyclone, and horizontal winds at 214 hPa (averaged 201 and 228 hPa) are shown as vectors. (b)

1 Vertical section of ERA40 vertical velocity averaged over 60°-150°E. Thick solid line  
2 is thermal tropopause derived from NCEP/NCAR reanalysis.

3 Figure 13. Vertical structures of July-August average (a) CAM3 vertical velocity ( $\text{mm s}^{-1}$ )  
4 averaged over 60°-150°E. Shaded regions indicate upward velocity (0.05, 0.1, 0.4, 0.7,  
5 1.0...mm/sec) and zero contour is shown as a dotted line. (b) Net radiative heating  
6 rates ( $\text{K day}^{-1}$ ) averaged over 60°-150°E. Contour interval is 0.2 for positive and 0.5 for  
7 negative values, respectively. Thin dashed lines denote isentropes (300, 320, 340, 360,  
8 380, and 500 K) and thick solid lines denote thermal tropopause. The topography is  
9 added at the bottom.

10

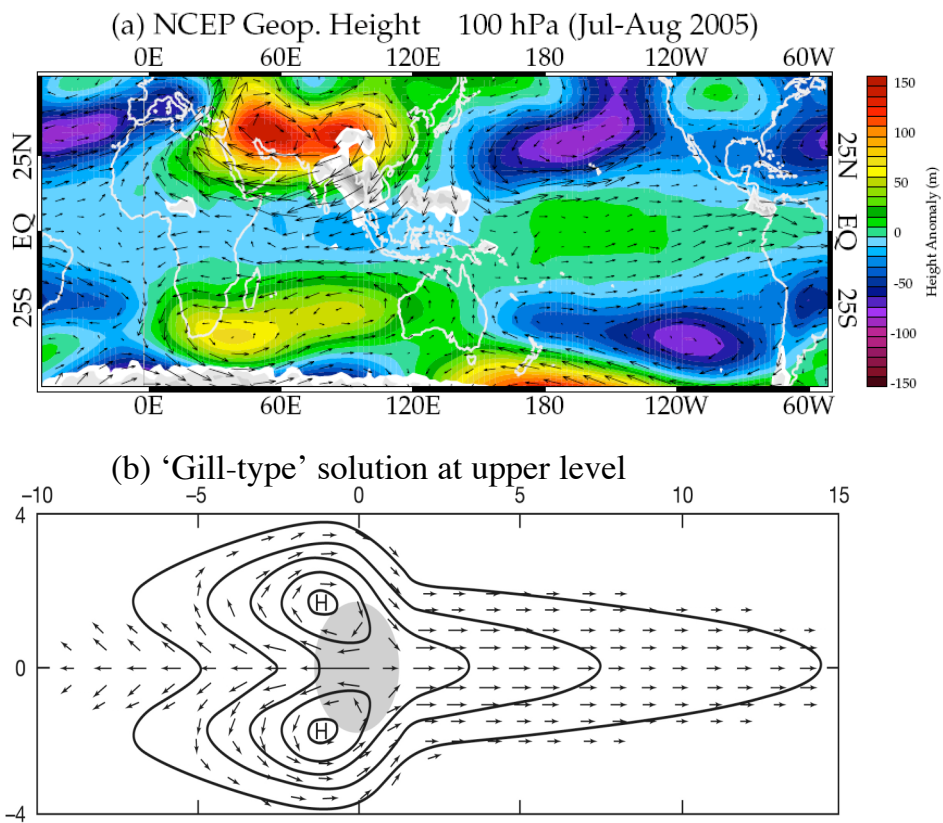
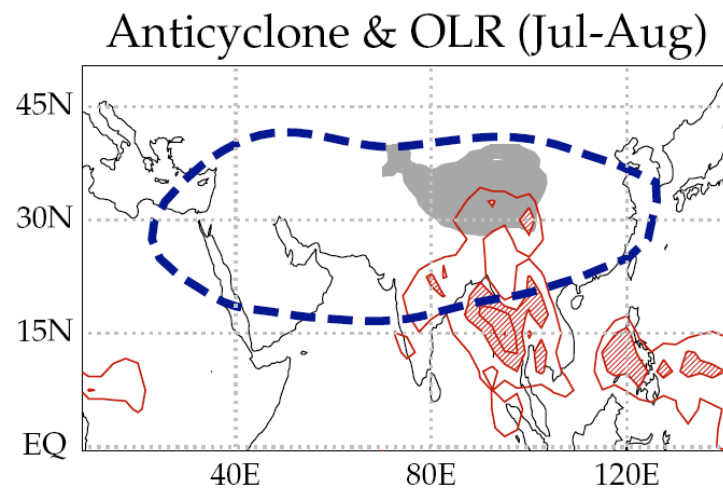


Figure 1

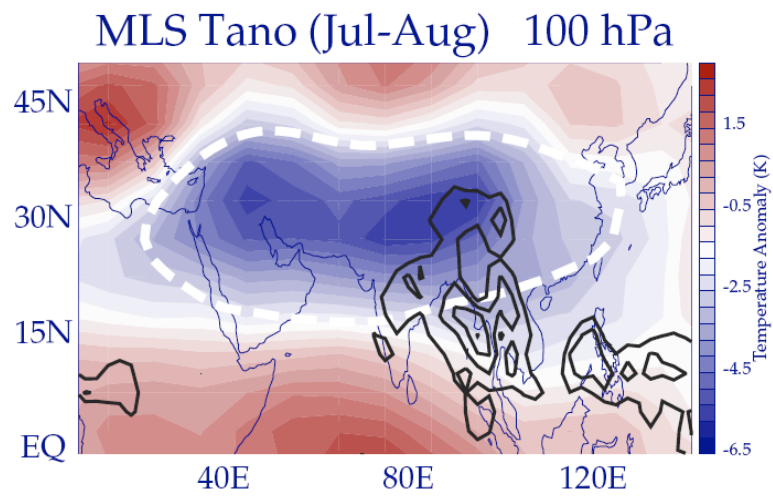
1  
2



3  
4  
5  
6  
7  
8

Figure 2

1  
2



3  
4  
5  
6  
7

Figure 3

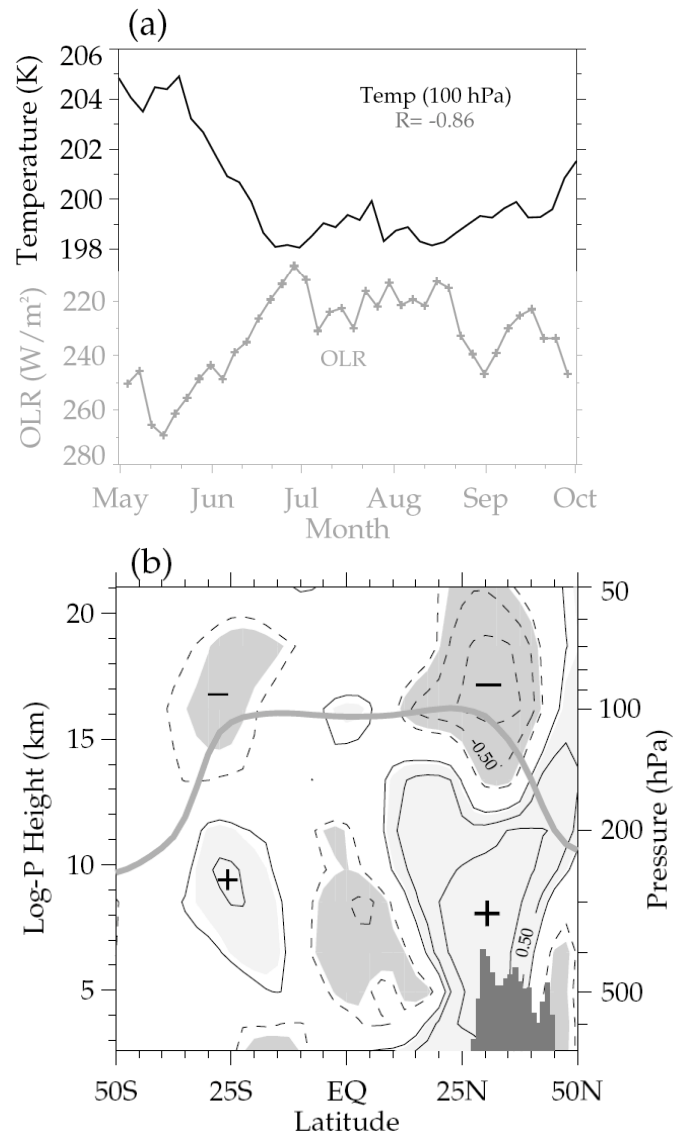


Figure 4



1

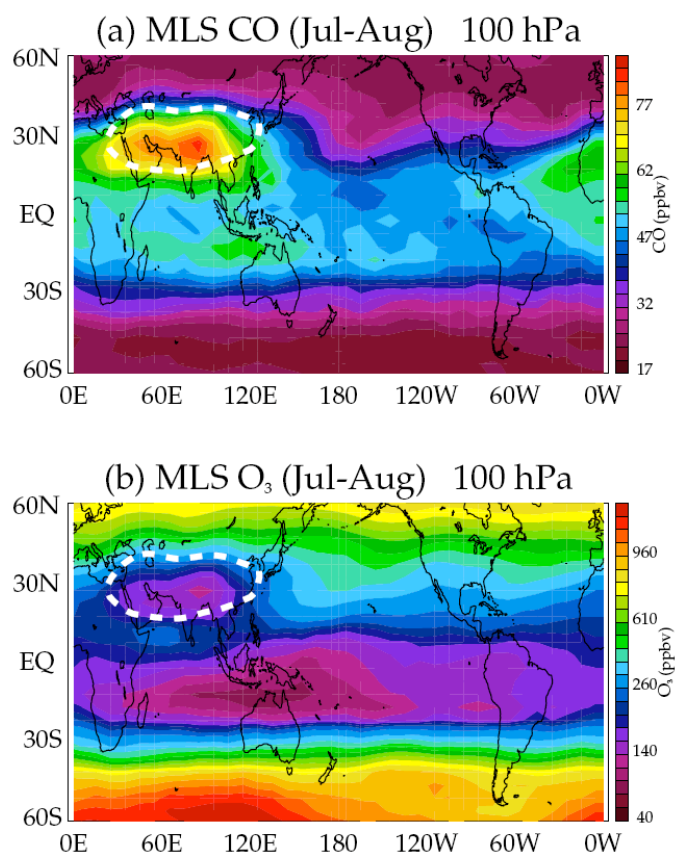
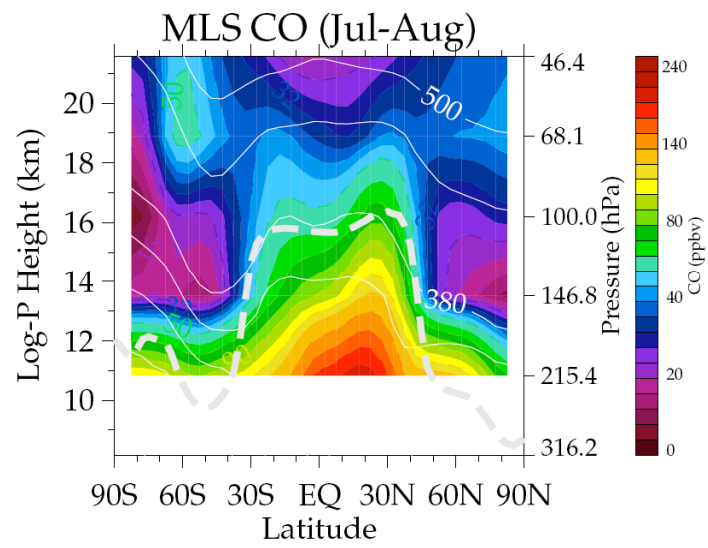


Figure 5

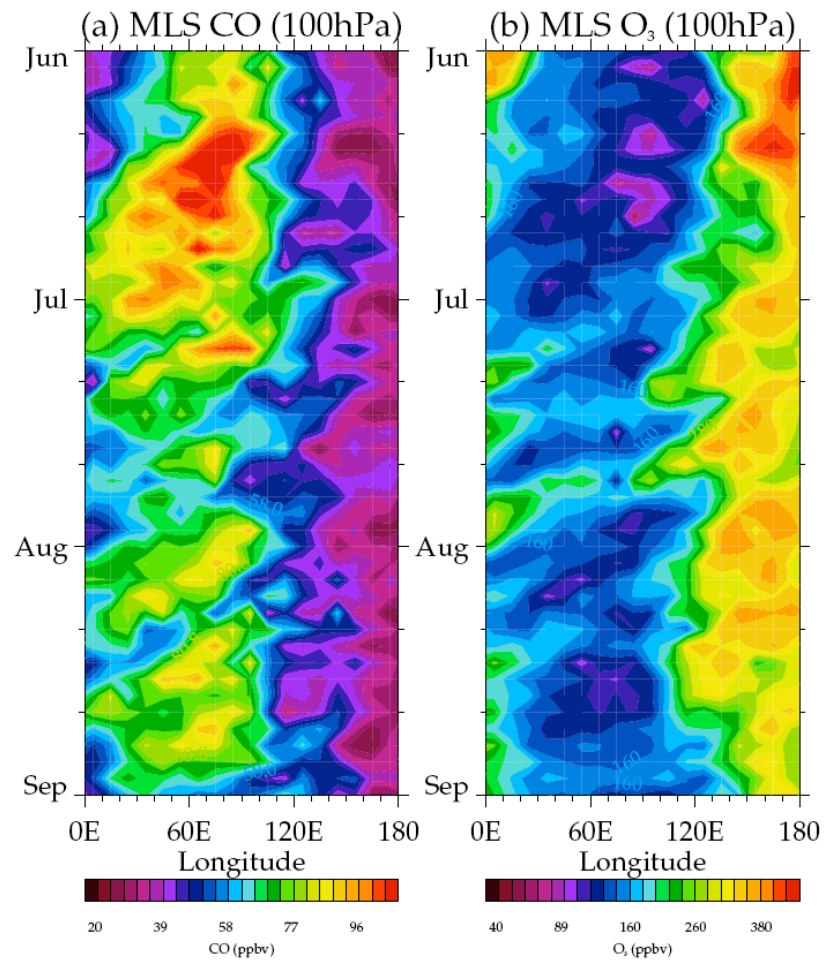
1  
2



3  
4  
5  
6  
7  
8

Figure 6

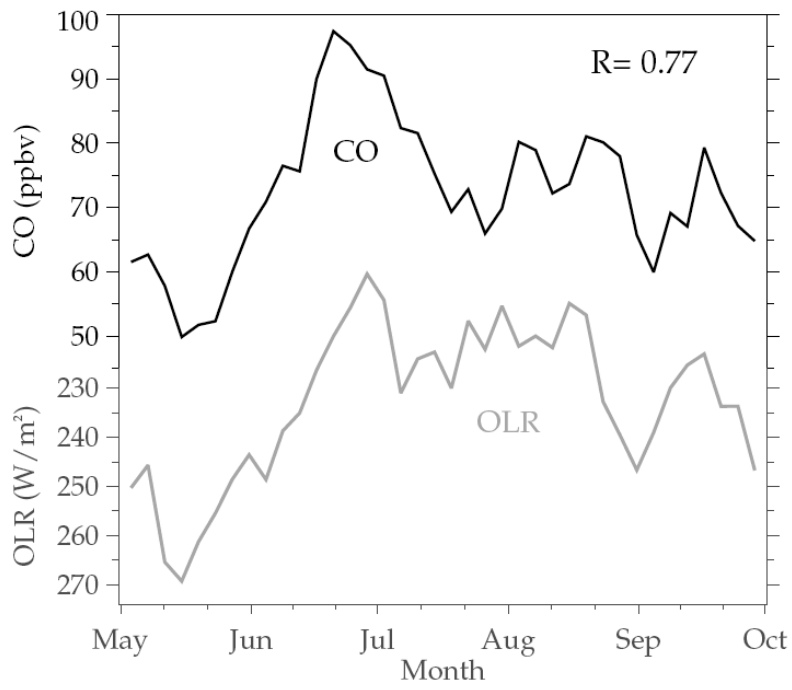
1  
2



3  
4  
5  
6  
7  
8

Figure 7

1  
2



3  
4  
5  
6  
7  
8

Figure 8

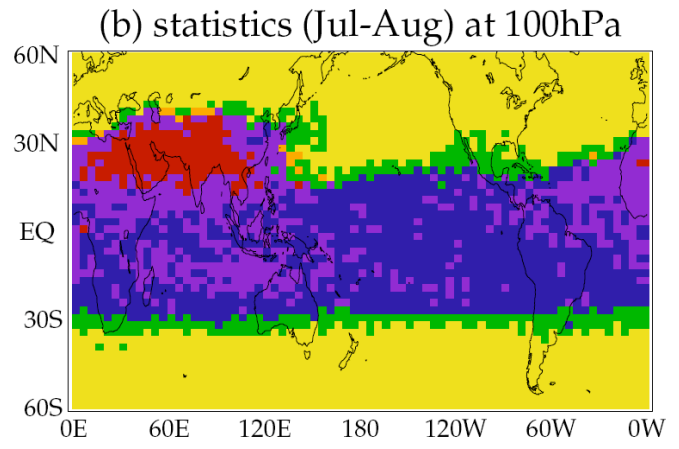
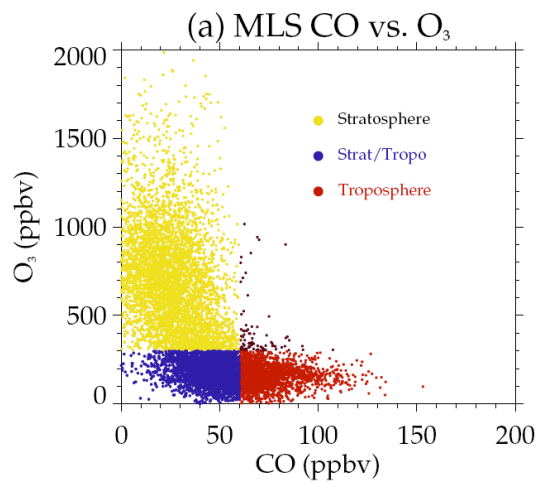
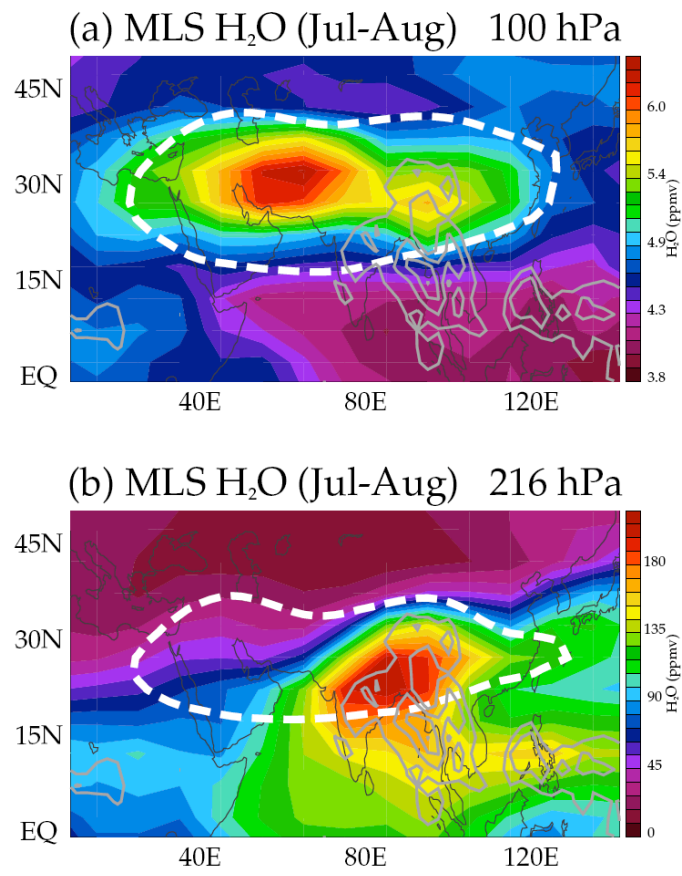


Figure 9

1



2

3

4

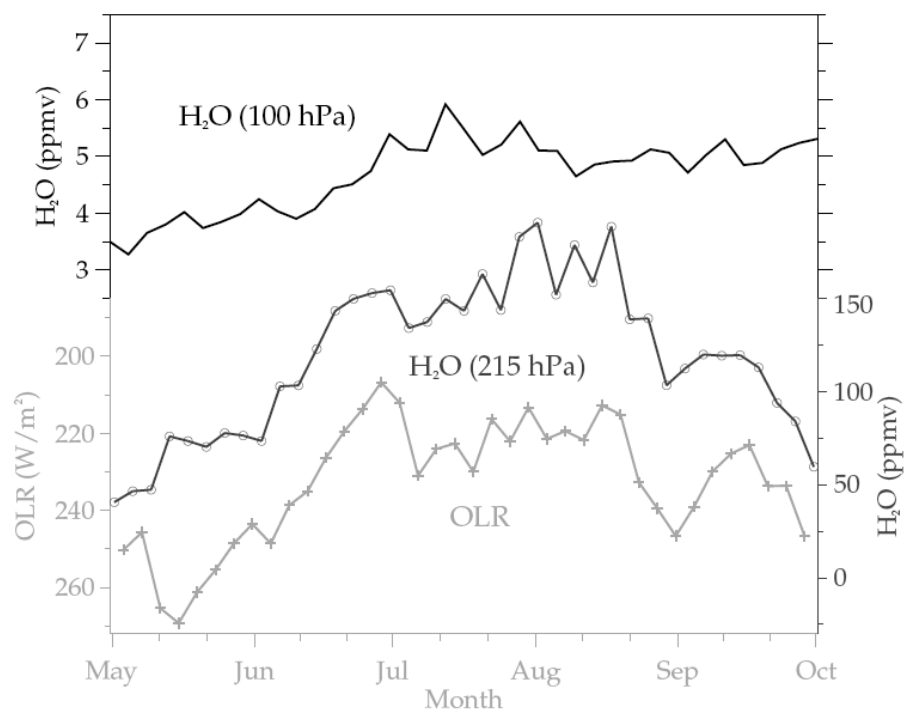
5

6

7

Figure 10

1  
2

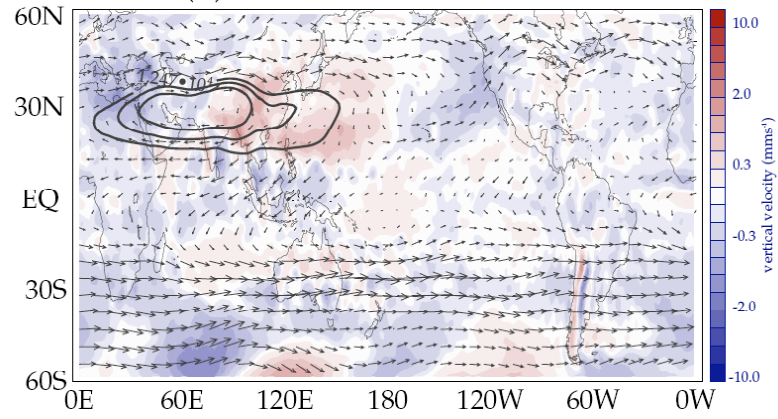


3  
4  
5  
6  
7  
8

Figure 11

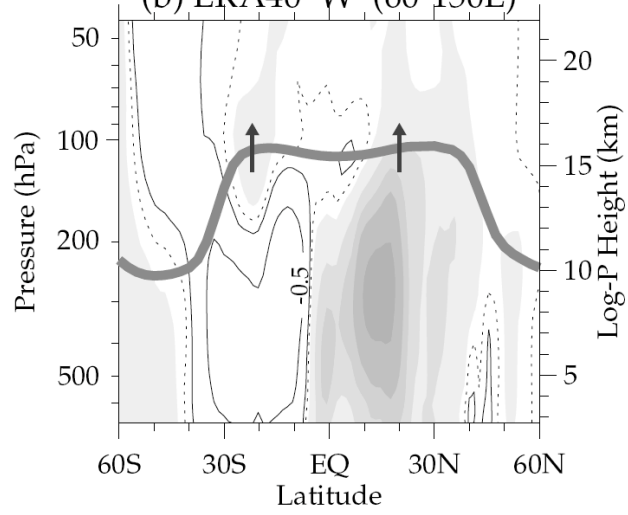
1  
2

(a) ERA40 W 104 hPa



3  
4

(b) ERA40 W (60-150E)

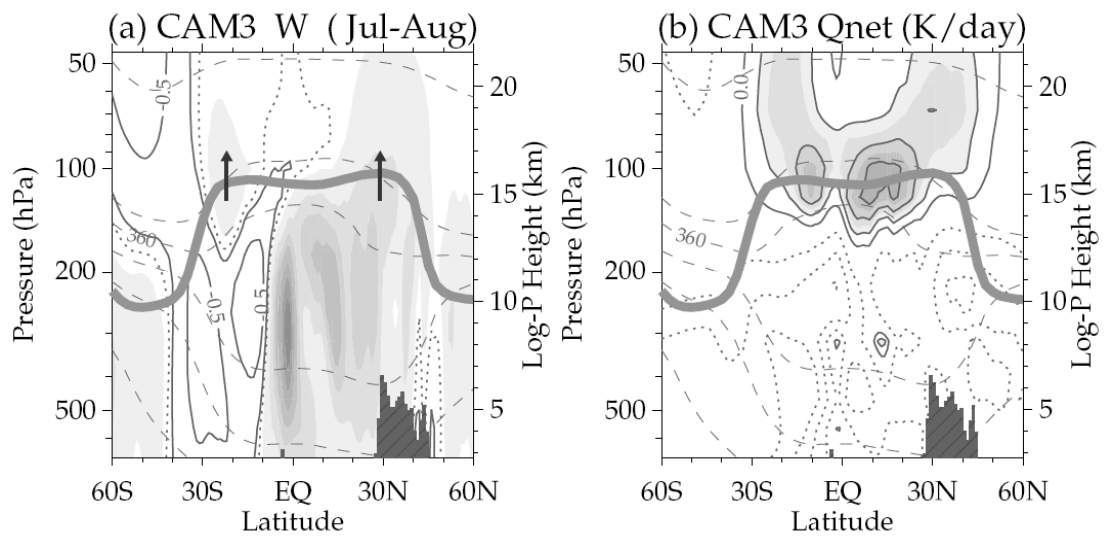


5  
6  
7  
8  
9  
10

Figure 12



1  
2



3  
4  
5  
6  
7  
8

Figure 13